CHEMISTRY OF MATERIALS
Article
pubs.acs.org/cm

Interaction of Pyridine and Water with the Reconstructed Surfaces of GaP(111) and CdTe(111) Photoelectrodes: Implications for CO_2 Reduction

Thomas P. Senftle,[†] Martina Lessio,[‡] and Emily A. Carter*[,†,§,∥]

[†]Department of Mechanical and Aerospace Engineering, Princeton University, Princeton, New Jersey 08544, United States
[‡]Department of Chemistry, Princeton University, Princeton, New Jersey 08544, United States
[§]Program in Applied and Computational Mathematics, Princeton University, Princeton, New Jersey 08544, United States
[∥]School of Engineering and Applied Science, Princeton University, Princeton, New Jersey 08544, United States

Supporting Information

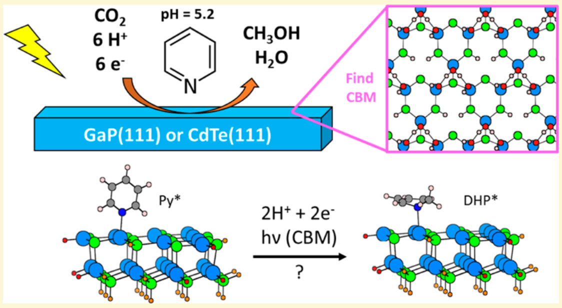

ABSTRACT: Pyridine (Py) is an effective cocatalyst during the photoelectrochemical reduction of CO_2 to methanol over GaP, CdTe, and $CuInS_2$ semiconductor surfaces. Identifying the role Py plays in the catalytic reduction mechanism is essential for optimizing the design of such photocatalytic processes. The Py-enhanced mechanism, however, is under considerable debate. Recent studies suggest that the semiconductor surface itself participates in a heterogeneous mechanism, and for this reason a detailed understanding of the interaction between Py and the surface is required. Additionally, surface reconstructions occurring during operation alter the nature of adsorption sites available for interaction with the solution, therefore impacting the performance of the electrode. To address this issue, we report a density functional theory investigation of the stability of GaP(111) and CdTe(111) surface reconstructions, as well as adsorption trends of intermediate species across sites created by such reconstructions. We also determine band edge positions of the solvated, reconstructed surfaces, which we compare to calculated reduction potentials involved in proposed elementary steps of the overall CO_2 reduction mechanism. This allows us to determine which reduction steps are thermodynamically feasible based on the energy of a photoexcited electron in the conduction band of the semiconductor. Given the band edge alignment of the GaP(111) surface, we determine that the 1e^- reduction of the solvated pyridinium cation most favorably results in the formation of adsorbed Py* + H* species and that the formation of a 1-pyridinyl radical in solution is unlikely. Furthermore, we find that it is thermodynamically feasible to form a newly proposed adsorbed 2-pyridinyl intermediate adsorbed on the surface, which may act as a powerful hydride donor. On the CdTe(111) surface, we find that no 1e^- reductions are thermodynamically feasible, leaving only 2e^- reductions leading to the formation of dihydropyridine (DHP) as possible reduction steps. These results identify stable intermediate species along the CO_2 reaction path over reconstructed surfaces, thus lending insight into the Py-catalyzed reaction mechanism.

1. INTRODUCTION

The photoelectrocatalytic reduction of CO_2 is a promising route to generate carbon-neutral fuels and value-added chemicals by using energy harnessed from sunlight.[1] Currently, such technologies generally suffer from low current densities and Faradaic efficiencies, rendering them impractical for large scale application. Encouragingly, recent experimental evidence suggests that pyridine (Py) can act as a cocatalyst during CO_2 reduction over various semiconductor surfaces, where its presence in the electrochemical cell lowers the applied potential required to achieve reduction, while at the same time enhancing Faradaic efficiency. Employing an illuminated p-GaP photocathode, Bocarsly and co-workers[2,3] achieved CO_2 reduction to methanol at near 100% Faradaic efficiency while operating at modest *underpotentials* (of ~300 mV). In addition to GaP electrodes, Py-enhanced photoreduction has recently been reported over CdTe[4] and $CuInS_2$[5−7] electrodes. In all cases, experiments have demonstrated that increased activity is correlated with the presence of Py at a solution pH of 5.2, indicating that the protonated pyridinium (PyH^+) species with a pK_a of 5.3 likely plays a role in achieving selective CO_2 reduction at such low potentials. This observation suggests that $PyH^+_{(aq)}$ may act in some way as an electron shuttle, facilitating the transfer of photoexcited electrons from the semiconductor surface to the reactant CO_2 molecule. Understanding the interaction between Py/PyH^+ and the semiconductor surface therefore is essential to optimizing this promising photoelectrochemical system for reducing CO_2 to energy-dense products.

Received: May 23, 2016
Revised: July 21, 2016
Published: July 22, 2016

ACS Publications

DOI: 10.1021/acs.chemmater.6b02084
Chem. Mater. 2016, 28, 5799−5810

The mechanism of Py-catalyzed CO_2 reduction is still under considerable debate. Bocarsly and co-workers[3] originally proposed that the initial reaction step features a one-electron ($1e^-$) reduction of $PyH^+_{(aq)}$ to a 1-pyridinyl ($1\text{-}PyH^{\bullet}_{(aq)}$) radical species at −0.6 V (vs SCE), where the reduction takes place in solution and the electrode acts only as an electron source (Scheme 1A). The $1\text{-}PyH^{\bullet}_{(aq)}$ radical, it was proposed, would then react with CO_2 to form a carbamate radical adduct, with subsequent reductions leading to methanol production. Theoretical studies by Tossel[8] and Keith and Carter,[9,10] however, showed that the $1e^-$ reduction of $PyH^+_{(aq)}$ to $1\text{-}PyH^{\bullet}_{(aq)}$ should occur at a far more negative potential of −1.44 V (vs SCE). This led to the subsequent[11] proposal that a two-electron ($2e^-$) reduction of Py to dihydropyridine (DHP) might occur instead, because the calculated reduction potential, −0.72 V (vs SCE), to form DHP is much closer to the experimentally applied potential. Given the theoretical[12] prediction, and subsequent experimental[13] observation, that H_2O can readily dissociate on the GaP surface to form a hydride-like species, it was proposed that a surface-bound DHP species could form from the reaction of adsorbed Py and a surface hydride.[14,15] Surface-bound DHP could then serve as the active catalytic intermediate for reaction with CO_2 through a concerted proton-coupled-hydride-transfer (PCHT) mechanism. The involvement of a DHP intermediate in a sequential hydride-transfer/proton-transfer (HT-PT) mechanism has also recently been suggested by Musgrave and co-workers,[16,17] with the proposal that DHP forms in solution through a series of sequential electron and proton transfers (ET-PT) proceeding through the aqueous $1\text{-}PyH^{\bullet}_{(aq)}$ radical (Scheme 1B). Additionally, Batista and co-workers have proposed that, on Pt electrodes, $PyH^+_{(aq)}$ is reduced to $Py_{(aq)}$ and an adsorbed hydride, which in turn may reduce CO_2 through a PCHT utilizing a surface hydride and an H^+ from $PyH^+_{(aq)}$ (Scheme 1C).[18−20] In this mechanism, however, $PyH^+_{(aq)}$ acts only as a Brønsted acid, which does not explain why an acidic environment alone fails to produce enhanced CO_2 reduction.

Scheme 1. Proposed Py-Catalyzed Reduction Paths Initiated with a $1e^-$ Reduction of $PyH^+_{(aq)}$ from Solution[a]

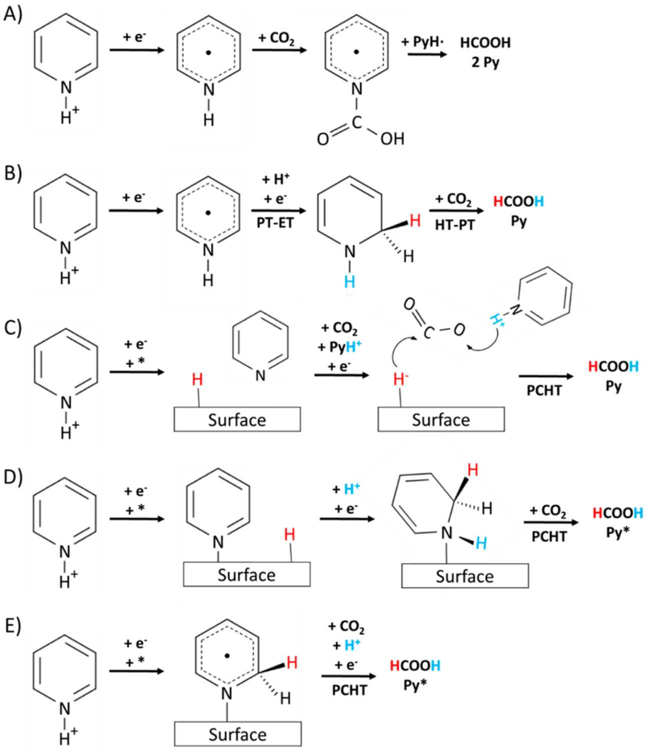

[a] Schemes A and B occur solely in solution, while schemes C−E require a surface-bound species. A * symbol represents an open surface site. Hydridic and protic hydrogens are indicated in red and blue, respectively.

Motivated by the mechanism suggested by Batista and co-workers, Lessio and Carter[21] investigated various $1e^-$ reductions of $PyH^+_{(aq)}$ that result in the formation of an adsorbed hydride on the GaP(110) surface. They found that reduction of $PyH^+_{(aq)}$ to adsorbed Py* + H* (where * indicates an adsorption site) is the most thermodynamically favorable, thus forming the precursors of the surface-bound DHP mechanism proposed by Keith and Carter (Scheme 1D). It was also recently suggested that a $1e^-$ reduction of $PyH^+_{(aq)}$ to an adsorbed 2-pyridinyl ($2\text{-}PyH^{\bullet}*$) radical species may be feasible (Scheme 1E), and that such a species could be a powerful hydride donor.[22] Since $2\text{-}PyH^{\bullet}*$ formation only requires a $1e^-$ reduction relative to $PyH^+_{(aq)}$, its involvement could explain CV evidence[20] that demonstrates a $1e^-$ reduction occurs on Pt electrodes rather than the $2e^-$ reduction required to form DHP. However, results indicating that a $1e^-$ reduction occurs on a Pt electrode, which is known to facilitate a $PyH^+ \rightarrow Py_{(aq)}$ + H* reduction,[19] do not necessarily preclude mechanisms involving $2e^-$ reductions over semiconductor electrodes. Here, we investigate the thermodynamic feasibility of the proposed $PyH^+_{(aq)}$ reductions, summarized in Scheme 1, on reconstructed GaP and CdTe surfaces in order to better understand which reduction steps may play a role in the CO_2 reaction mechanism over semiconductors.

Numerous proposed reaction steps involve the adsorption of Py-derived species, suggesting that the rate of such steps can be tuned by altering the nature of adsorption sites exposed on the electrode surface. This appears to be the case, as a number of experimental reports implicate the electrode in a heterogeneous mechanism, where the performance of the electrode can be affected by alterations in the surface morphology. Recently, Hu and Bocarsly observed[23] increased current densities on electrodes prepared with GaP(110) facets exposed by chemical etching of the GaP(111) surface. They demonstrated a correlation between exposed (110) surface area and overall current density, suggesting that the difference in activity stems from varying adsorbate interaction strengths between the two facets. Understanding this facet dependence can offer insight into the mechanism at play, as well as inform design choices leading to more effective photoelectrodes. Additionally, studies employing CdTe[4] and $CuInS_2$[6,7] electrodes report a poisoning effect at high $Py_{(aq)}$ concentrations, where CO_2 reduction is inhibited after a critical $Py_{(aq)}$ concentration is reached. This effect suggests that Py-derived intermediates specifically adsorb on the surface, which can poison active reduction sites at sufficiently high coverages. Since Py adsorption strength can vary between surfaces, the magnitude of Py poisoning will also vary, therefore leading to facet-dependent performance. Given this evidence demonstrating the importance of available surface sites, we contend that the Py-catalyzed reaction mechanism involving the semiconductor electrodes studied to this point is most likely heterogeneous in nature, with active participation of the electrode surface.

In this work, we consider GaP and CdTe electrode surfaces, since these materials share a common zinc-blende crystal structure,[24] allowing for direct comparisons at equivalent adsorption sites. During operation, the electrode surface will evolve to a stable structure in equilibrium with its environment,[25] affecting which adsorption sites are available to species in the solution. Such evolution is particularly important when considering active sites on GaP(111) and CdTe(111) surfaces (i.e., the predominant facets exposed in the CO_2 reduction experiments[2,4,23]), which are inherently polar and therefore are prone to reconstruction.[25] We identify which surface structures are likely present during catalytic operation by employing the formalism of *ab initio* thermodynamics to compute the relative free energy of possible surface reconstructions (section 3.1). We then investigate the interaction of the reconstructed surfaces with solvating H_2O molecules, allowing us to calculate band edge positions of the solvated electrodes (section 3.2). Cluster models of the reconstructed surfaces, utilizing an implicit solvation scheme, are then used to calculate the redox potentials of proposed $PyH^+_{(aq)}$ reduction steps (section 3.3). Comparing the band edge positions of the solvated surfaces to the calculated reduction potentials allows us to determine which steps are feasible through the transfer of photoexcited electrons from the semiconductor, and thus which steps are most significant to the Py-enhanced reduction mechanism. Such information will help improve the design of photocathodes to take full advantage of Py cocatalysis, as well as aid the search for other photoelectrode/organic-molecule systems with similar synergism.

2. METHODS

Periodic density functional theory (DFT) calculations were computed using the Vienna *ab initio* simulation package (VASP 5.3.2).[26] The generalized gradient approximation (GGA) for exchange-correlation (XC) was employed, as implemented in the Perdew−Burke−Ernzerhof (PBE) formulation.[27] The Grimme D2[28] empirical correction scheme was included in all calculations to capture dispersion interactions. Default projector augmented wave (PAW) potentials[29] were used to represent the nuclei and frozen core electrons. The following valence electrons were treated self-consistently: Ga ($4s^24p^1$), P ($3s^23p^3$), Cd ($4d^{10}5s^2$), Te ($5s^25p^4$), N ($2s^22p^3$), O ($2s^22p^4$), C ($2s^22p^2$), and H ($1s^1$). All calculations were spin-polarized, with a kinetic energy cutoff of 600 eV to truncate plane-wave basis sets during geometry optimizations and frequency calculations. Final energies were further refined with a single-point calculation employing a cutoff of 800 eV. Monkhorst−Pack (MP)[30] Brillouin zone sampling was used to generate 4 × 4 × 1 and 2 × 2 × 1 k-point spacing schemes for (2 × 2) and (4 × 4) periodic slab unit cells, respectively. The Brillouin zone was integrated with the Gaussian smearing method employing a smearing width of 0.05 eV. In all cases, a vacuum layer of at least 15 Å was included to separate periodic slab images, with a dipole correction included to eliminate spurious slab−slab interactions. The employed computational parameters resulted in total energies converged to within 1 meV per stoichiometric formula unit of the semiconductor. Calculations involving isolated gas phase molecules were treated in a 15 Å × 15 Å × 15 Å simulation cell with no k-point sampling. The band gap of bulk CdTe was calculated with the non-self-consistent G_0W_0 method,[31,32] utilizing a DFT ground-state electron density obtained with the PBE functional. This calculation, performed on a primitive (1 × 1) bulk CdTe unit cell, included 256 bands and 96 frequency points. The Brillouin zone was sampled with a Γ-point-centered 8 × 8 × 8 k-point grid, which was sufficient to converge the obtained band gap to within 0.1 eV. All reported Gibb's free energies were calculated as $G = E_{0K} + \text{ZPVE} + \Delta H(0\text{ K} \rightarrow 298\text{ K}) - T{\cdot}\Delta S(0\text{ K} \rightarrow 298\text{ K})$, where well-established statistical mechanical expressions were used to calculate translational, rotational, and vibrational energies and entropies (ZPVE is the zero-point vibrational energy). Only vibrational contributions were included for surfaces and adsorbates on surfaces, since such extended systems have no translational or rotational degrees of freedom.

Slab models of the zinc-blende GaP(111) and CdTe(111) surfaces consisted of (2 × 2) unit cells with five cation−anion (i.e., Ga−P or Cd−Te) bilayers containing eight cation−anion formula units per layer, as shown in Figure 1. Test calculations employing seven bilayers demonstrated that five bilayers are sufficient to yield surface energies converged to within 2 meV $Å^{-2}$. Lattice parameters were determined from separate optimizations of the zinc-blende bulk unit cell of each material modeled with a primitive unit cell and 8 × 8 × 8 MP k-point sampling. Optimization resulted in lattice constants of 5.45 and 6.61 Å for GaP and CdTe, respectively, in agreement with the respective experimental[24] values of 5.45 and 6.48 Å. Cleaving a stoichiometric (111) zinc-blende surface results in a polar geometry, and as such we employed a pseudohydrogen capping scheme to saturate dangling bonds associated with under-coordinated P or Te atoms exposed on the reverse side of the slab (Figure 1).[25] In this scheme, a noninteger core charge, *Z*, is assigned to each pseudohydrogen based on the valence electron number of the atom replaced by the pseudohydrogen, where each pseudohydrogen contributes *Z* electrons to retain a neutral system. Ga and Cd have three and two valence electrons, respectively, that are divided over four bonds in the bulk zinc-blende structure, and thus pseudohydrogens with positive core-charges of $Z = 3/4e$ and $Z = 2/4e$, respectively, are required to saturate dangling bonds on the reverse side of the slab. Each pseudohydrogen was placed in the next cation crystallographic position below the slab and then was allowed to relax along its bond relative to the fixed slab. The top two bilayers, along with any adsorbates, were relaxed using a conjugate gradient force minimization scheme, where frequency analyses were completed to ensure that an energy minimum was obtained in each case. The bottom three bilayers were held fixed in their bulk positions. Test calculations modeling lower adsorbate coverages employed a larger (4 × 4) unit cell, which contained three bilayers with only the bottom bilayer held fixed during geometry optimization.

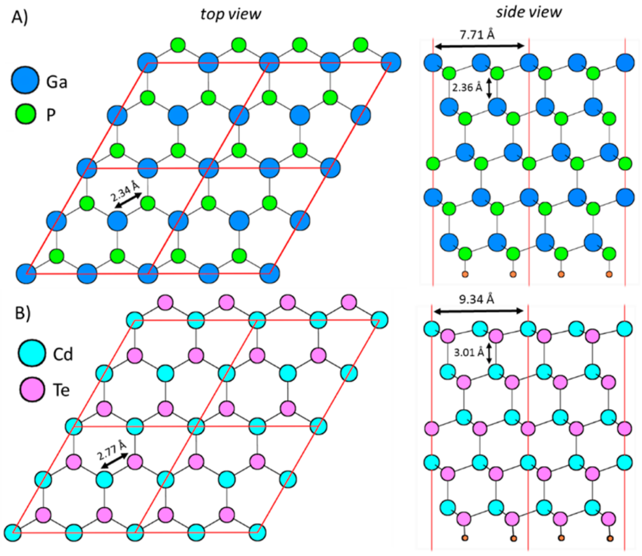

Figure 1. Periodic models of the stoichiometric (A) GaP(111) and (B) CdTe(111) surfaces. Orange circles represent pseudohydrogen saturators, where $Z = 3/4e$ in A and $Z = 2/4e$ in B. Subsurface atoms are omitted for clarity in the top view perspectives.

Calculations employing cluster models were computed using the NWCHEM 6.6 simulation package.[33] The hybrid B3LYP[34,35] XC functional was employed in all calculations, along with D2[28] dispersion corrections. Benchmark calculations employing the PBE[27] XC functional were also conducted to validate the cluster model approach against periodic VASP calculations. Implicit solvation was included using the continuum solvation model based on solute electron density (SMD),[36] with NWCHEM default parameters for the water dielectric constant (ε = 78.4) and all atomic radii. Ga, Cd, and Te were described with Stuttgart (28, MWB), Stuttgart (28, MWB), and Stuttgart (46, MWB) effective core potentials and corresponding basis sets, where Ga ($4s^2 4p^1$), Cd ($4s^2 4p^6 4d^{10} 5s^2$), and Te ($5s^2 5p^4$) valence electrons were treated self-consistently.[37,38] All other atoms were treated with the Pople all-electron 6-31G** basis set[39] for geometry optimization and frequency calculations, and with the Dunning all-electron aug-cc-pVDZ basis set[40] for refined single-point energy calculations. Minimum energy structures were confirmed by ensuring that all imaginary vibrational frequencies were eliminated.

Cluster models of the GaP(111) and CdTe(111) surfaces were cleaved from optimized periodic structures of (2 × 2) reconstructed surfaces centered at a Ga/Cd vacancy (Figure 2), where the use of this particular reconstruction is explained in section 3.1. This results in a total of 24 P/Te atoms (12 in the surface layer, 12 in the subsurface layer) and 21 Ga/Cd atoms (9 in the surface layer, 12 in the subsurface layer), where in the surface layer there is one Ga/Cd vacancy per four P/Te atoms. The number of surface Ga/Cd-sp^2 sites equals the number of surface P/Te-sp^3 sites, which ensures that electrons from all dangling Ga/Cd bonds are donated to fill dangling P/Te bonds (i.e., to form an empty p orbital on the cation and a lone pair on the anion). This stoichiometry is required to obtain a stable semiconducting surface, as discussed further in section 3.1. Building on a methodology previously developed for a cluster model of the GaP(110) surface,[10,21] we employ a modified hydrogen capping scheme to saturate innocent dangling bonds at the cluster boundary. Modification of the capping scheme used in ref 10 was necessary because the scheme, while applicable to the covalent GaP solid, failed to treat the more ionic CdTe system. For this reason, we employed a pseudohydrogen capping scheme, as was done on the periodic slab models, to better capture the ionic character of Cd−Te bonds. Innocent dangling bonds thus were saturated by pseudohydrogens with core charges determined from the valence electron number of each atom type: $Z = 3/4e$, $Z = 5/4e$, $Z = 2/4e$, and $Z = 6/4e$ when replacing Ga, P, Cd, and Te, respectively. The chosen cluster stoichiometry, and application of pseudohydrogen saturators, yields a neutral system in a singlet spin state. For the GaP system, the pseudohydrogen capping scheme performs very similarly to the regular-hydrogen capping scheme, as further discussed in the Supporting Information. Thus, the pseudohydrogen scheme was used throughout this work for consistent comparison to the CdTe system, for which the regular-hydrogen capping scheme fails. Pseudohydrogens were initially placed by allowing their bond lengths to relax relative to the fixed cluster and were then held frozen during subsequent geometry optimizations of all other cluster and adsorbate atoms. Adsorption energies and geometries obtained with cluster models were benchmarked against periodic calculations, which demonstrated satisfactory agreement between the two approaches. Again, statistical mechanical expressions were employed to derive vibrational, translational, and rotational thermochemical properties, where only vibrational contributions are included in cluster calculations representing a surface with no translational or rotational degrees of freedom.

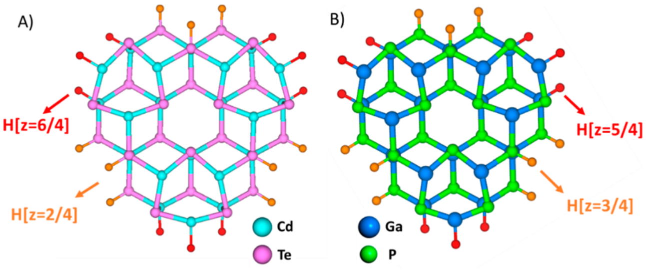

Figure 2. Cluster models of the reconstructed (A) CdTe(111) and (B) GaP(111) surfaces. Red and orange spheres represent pseudohydrogen saturators replacing anions and cations, respectively, where core charges are defined as labeled in the figure.

Using the cluster models, we report computed redox potentials of possible reduction steps leading to the formation of Py-derived intermediates adsorbed on the electrode surfaces. All reduction potentials are calculated from reaction free energies in solution using previously established methods.[9,10] The reduction potential is calculated with the equation:

$$E^0 = \frac{-\Delta G_{aq}}{nF} - \frac{m\cdot RT\ \ln(10)}{n}\text{pH} \qquad (1)$$

where E^0 is the reduction potential, n is the number of electrons transferred in the reduction, m is the number of protons involved in the reaction, F is the Faraday constant, R is the gas constant, T is the temperature (T = 298 K), and ΔG_{aq} is the reaction free energy in solution. ΔG_{aq} is calculated from the equation:

$$\Delta G_{aq} = G_{Red} - G_{Ox} - n\cdot G_{e^-} - m\cdot G_{H^+} \qquad (2)$$

where G_{Red} and G_{Ox} are the free energies of the reduced and oxidized species in solution (including all relevant translational, rotational, and vibrational contributions), G_{e^-} is the free energy of an electron in solution, and G_{H^+} is the free energy of a proton in solution. G_{e^-} is

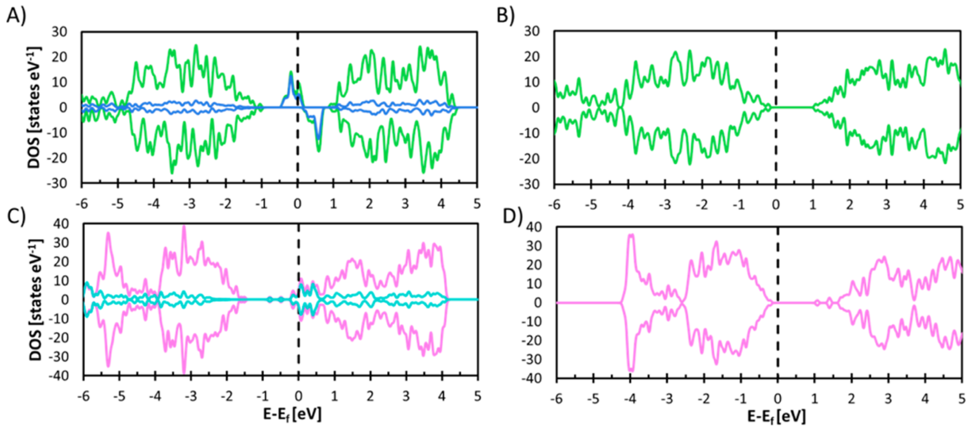

Figure 3. (A,B) DOS of the GaP(111) surface (A) before and (B) after Ga vacancy formation. Green data correspond to the total DOS, and blue data correspond to the PDOS of surface Ga atoms. (C,D) DOS of the CdTe(111) surface (C) before and (D) after Cd vacancy formation. Pink data correspond to the total DOS, and light blue data correspond to the PDOS of surface Cd atoms. The vertical dashed line corresponds to the Fermi level.

determined from an empirical value for the absolute potential of the standard hydrogen electrode (SHE = −4.281 eV),[41] and for G_{H^+} we employ an empirical value of −11.72 eV.[42] We report all reduction potentials versus the standard calomel electrode (i.e., −0.244 V SCE relative to 0 V SHE) and calculated at pH = 5.2 to correspond to the electrochemical conditions of the reported CO_2 reduction experiments.

3. RESULTS AND DISCUSSION

3.1. Surface Reconstructions. The (111) facets of zinc-blende crystals are intrinsically polar and therefore are prone to surface reconstructions.[43] The issue of surface reconstruction is of particular interest in this study, as the CO_2 reduction experiments reported by Bocarsly and co-workers[2,23] were conducted on a photoelectrode exposing a GaP(111) single-crystal surface. Similarly, X-ray diffraction of the CdTe thin-film electrode employed by Jeon et al.[4] indicated a dominant (111) crystal orientation. The stoichiometric termination of both surfaces, shown in Figure 1, exposes dangling cation bonds that lead to the occupation of high energy states in the conduction band (CB).[25] This is demonstrated by the density of states (DOS) of both surfaces shown in Figure 3A and C, where high energy states of the CB are shifted below the Fermi level. A projected DOS (PDOS) analysis of each surface further demonstrates that the occupied CB states are localized on Ga and Cd atoms at the surface. Hence, surface reconstructions that eliminate dangling bonds will be thermodynamically favored by shifting the associated high energy states above the Fermi level.

We identify reconstructions that adequately remove all dangling bond states by using electron counting (EC) rules,[44] where we follow a methodology previously applied by Scheffler and co-workers to predict stable reconstructions of GaAs surfaces.[25,44,45] EC rules use the valence of each atom type to assign the fractional number of electrons supplied to each bond by that atom type. This information can then be used to determine the total number of electrons (per unit cell) that occupy high-energy states in an unstable surface termination, thus determining the number of electrons that must be removed by the reconstruction. Since each atom forms four bonds in the zinc-blende crystal structure, Ga formally contributes $3/4e^-$ and Cd contributes $2/4e^-$ to each bond. There are four Ga dangling bonds exposed per (2 × 2) unit cell of the stoichiometric surface, resulting in a total of $3e^-$ that must be removed from the CB. Analogously, there are a total of $2e^-$ occupying high-energy states of the stoichiometric CdTe(111) surface. Reconstructions resulting in a net $3e^-$ oxidation of the (2 × 2)-GaP(111) surface and a $2e^-$ oxidation of the (2 × 2)-CdTe(111) surface therefore will be stable.

On both surfaces, the required oxidation can be accomplished by creating one neutral Ga or Cd atom vacancy per (2 × 2) unit cell, as shown in Figure 4. The DOS of the reconstructed surfaces, shown in Figure 3B and D, confirm that high-energy states of the CB are no longer occupied. This is in agreement with theoretical predictions (from DFT)[25,46] and experimental observations (from low-energy electron diffraction)[47] reported in the literature demonstrating the stability of a similar reconstruction on the related GaAs(111) surface. In addition to Ga or Cd vacancy formation, the surface can be "oxidized" by adsorbing additional P or Te adatoms as monomers or trimers (Figure 5). Both theoretical[48] and experimental[49] reports in the literature demonstrate that the (2 × 2) Cd-vacancy reconstruction of CdTe(111) is thermodynamically stable, and as such we do not consider reconstructions involving Te adatoms in the present study. However, similar studies are not yet available for the GaP(111) surface, so we use *ab initio* thermodynamics to determine which reconstruction is most stable since multiple reconstructions of this surface are feasible.

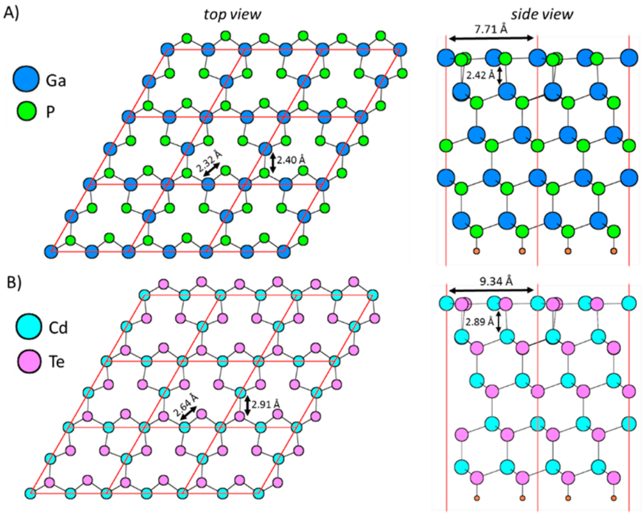

Figure 4. Periodic models of (2 × 2) reconstructions of the (A) GaP(111) and (B) CdTe(111) surfaces containing one surface Ga or Cd vacancy per unit cell. Orange circles represent pseudohydrogen saturators, where $Z = 3/4e$ in A and $Z = 2/4e$ in B. Subsurface atoms are omitted for clarity in the top view perspectives.

We define the free energy of a surface reconstruction relative to a bulk reservoir for each atom type following the methodology described by Moll et al.[25] for application to GaAs(111) and subsequently applied by Li et al.[48] to CdTe(111). For GaP, the free energy difference separating possible reconstructions is defined relative to the chemical potential of Ga and P using the following equation:

$$\Delta\gamma_{1\to2} = \Delta G_{1\to2} - \Delta N^{\mathrm{Ga}}_{1\to2}(G^{\mathrm{bulk}}_{\mathrm{GaP}} - \mu_{\mathrm{P}}) - \Delta N^{\mathrm{P}}_{1\to2}\mu_{\mathrm{P}} \tag{3}$$

where $\Delta\gamma_{1\to2}$ is the surface energy difference between surfaces 1 and 2 relative to bulk Ga and P reservoirs, $\Delta G_{1\to2}$ is the difference in free energy between slab models, $\Delta N^{\mathrm{Ga}}_{1\to2}$ and $\Delta N^{\mathrm{P}}_{1\to2}$ are the respective differences in the number of Ga and P atoms per unit cell, $G^{\mathrm{bulk}}_{\mathrm{GaP}}$ is the free energy of bulk zinc-blende GaP per formula unit, and μ_{P} is the chemical potential of phosphorus. The chemical potential of Ga is implicitly included in eq 3 through the relation: $G^{\mathrm{bulk}}_{\mathrm{GaP}} = \mu_{\mathrm{P}} + \mu_{\mathrm{Ga}}$. The limits of μ_{P} and μ_{Ga} are set by the free energies of bulk phosphorus and gallium with the equations:

$$(G^{\mathrm{bulk}}_{\mathrm{P}} + \Delta G_{\mathrm{f}}) < \mu_{\mathrm{P}} < G^{\mathrm{bulk}}_{\mathrm{P}} \tag{4}$$

and

$$\Delta G_{\mathrm{f}} = G^{\mathrm{bulk}}_{\mathrm{GaP}} - G^{\mathrm{bulk}}_{\mathrm{Ga}} - G^{\mathrm{bulk}}_{\mathrm{P}} \tag{5}$$

where ΔG_{f} is the formation free energy of GaP relative to bulk Ga and P, $G^{\mathrm{bulk}}_{\mathrm{P}}$ is the free energy per atom of bulk white phosphorus[50] (Figure S1A), and $G^{\mathrm{bulk}}_{\mathrm{Ga}}$ is the free energy per atom of bulk orthorhombic gallium[51] (Figure S1B). Phase separation will occur at chemical potentials beyond the limits shown in eq 4, since either a bulk Ga or P phase will become more stable than the GaP surface phase. White phosphorus was

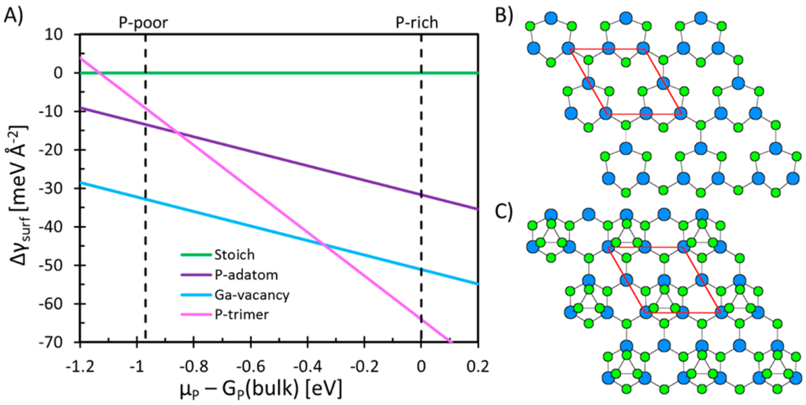

Figure 5. (A) Surface free energy of reconstructions calculated relative to the stoichiometric GaP(111) surface. (B,C) Top view of (B) a reconstruction with one Ga vacancy per unit cell and (C) a surface with one adsorbed P trimer per unit cell. Ga and P atoms are represented by blue and green circles, respectively. The unit cell is indicated by red lines, and only surface atoms are shown for clarity.

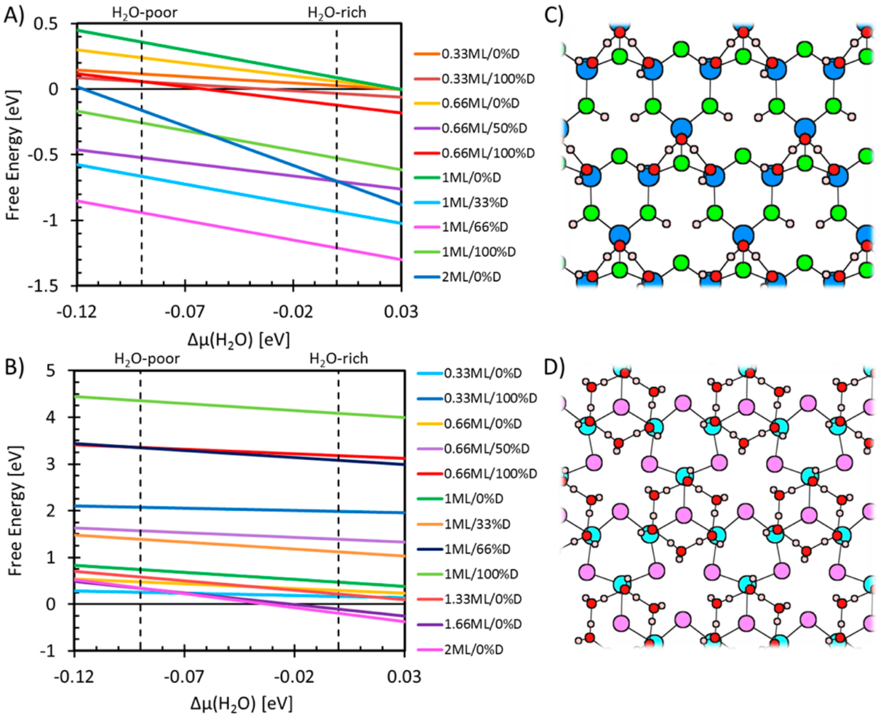

Figure 6. (A,B) Adsorption free energy at 298 K of water on the reconstructed (A) GaP(111) and (B) CdTe(111) surfaces. (C,D) Top view of the thermodynamically favored water adsorption/dissociation geometries on the (C) GaP(111) surface (at 1 ML and 66% dissociation) and (D) CdTe(111) surface (at 2 ML and 0% dissociation). Adsorption free energy is plotted against the chemical potential of water referenced to the H_2O-rich limit: $\Delta\mu(H_2O) = \mu(H_2O) - \mu(H_2O\text{-rich})$. Ga, P, Cd, Te, O, and H atoms are represented by dark blue, green, light blue, pink, red, and white circles, respectively. Only surface atoms are shown for clarity.

chosen as the reference for μ_P because it is the most readily formed phase of phosphorus. Although red and black phosphorus are energetically more stable, their formation is kinetically limited. Using red or black phosphorus as the reference will shift G_P^{bulk}, and therefore also the range of accessible μ_P, to a lower energy. This choice of reference does not impact any conclusions drawn herein, as will be discussed below. We also calculate a DFT heat of formation for bulk GaP of $\Delta H_f = -23.3$ kcal mol^{-1} relative to white phosphorus, in agreement with the experimental[24] value of $\Delta H_f = -21.0$ kcal mol^{-1}.

In Figure 5, we plot the free energy of surfaces reconstructed with a Ga vacancy, an adsorbed P adatom, and an adsorbed P trimer, all calculated relative to the stoichiometric surface. As seen in the figure, Ga vacancies are stable under P-poor conditions, while adsorbed P trimers are stable under P-rich conditions. This is in agreement with previously reported surface reconstructions on the similar GaAs(111) surface.[25,46] Hu and Bocarsly[23] reported an X-ray photoemission spectroscopy (XPS) composition analysis of the electrode surfaces used in their electrochemistry experiments, which demonstrated high Ga/P ratios of ~1.25 on the employed electrodes. Since the electrodes were P-deficient, we deem that the reconstructed surface with one Ga vacancy per (2 × 2) unit cell best represents the electrode surface under electrochemical conditions. Also, it is plausible that a Ga vacancy can act as a nucleation site for the formation of the trifold grooves reported by Hu and Bocarsly,[23] which is evident from the orientation of

DOI: 10.1021/acs.chemmater.6b02084
Chem. Mater. 2016, 28, 5799−5810

the surface channels opened by the Ga-vacancy reconstruction (Figure S2). Finally, if we had chosen red or black phosphorus as a reference, then the $\mu_P = G_P^{bulk}$ boundary would be shifted to a lower energy (i.e., shifted to the left in Figure 5A). This would cause the P-trimer surface to fall outside the range of feasible P chemical potential altogether, leaving only the reconstructed surface with Ga vacancies in the range of stability. We therefore use the Ga-vacancy reconstruction of GaP(111), as well as the analogous Cd-vacancy reconstruction of the CdTe(111) surface predicted theoretically with DFT by Li et al.[48] and observed experimentally with scanning tunneling microscopy (STM) by Egan et al.,[49] for the following investigations of water adsorption and $PyH^+_{(aq)}$ reduction.

3.2. Electrode Interaction with the Solvent: H_2O Adsorption and Dissociation.

Interactions between the electrode and the solvent, such as the adsorption and dissociation of water molecules, can significantly affect the band edge alignment of the semiconductor.[52,53] In this section, we determine the most stable structure of the semiconductor/water interface for both the reconstructed GaP(111) and CdTe(111) surfaces. These structures are then used to derive the position of each surface's conduction band minimum (CBM), which can then be directly compared to the reduction potentials of proposed $PyH^+_{(aq)}$ reduction steps. Reconstructions of both CdTe(111) and GaP(111) yield open sp^2 cation sites with empty p states, as well as sp^3 anion sites with exposed lone pairs. These sites are susceptible to donor−acceptor bonding interactions with water, where H_2O can adsorb through an O lone pair interaction at the Ga/Cd sp^2 site or can dissociate through an OH^- lone pair interaction at the Ga/Cd sp^2 site coupled with H^+ interaction at the P/Te sp^3 lone pair site (Figure 6). To model these interactions, we considered H_2O adsorption geometries varying from coverages of $\theta = 1/3$ monolayer (ML) to $\theta = 2$ ML (where $\theta = 1$ ML corresponds to one adsorbed H_2O molecule per sp^2 cation site) and with degrees of dissociation varying from 0% to 100%. The most stable configuration is then determined by plotting the adsorption free energy of each geometry against the chemical potential of water ($\mu(H_2O)$), defined by $\Delta G_{ads} = G_{surf/water} - G_{surf} - n(H_2O)\cdot\mu(H_2O)$, as was done for the GaP(110) surface in ref 13. The H_2O-rich and -poor limits shown in Figure 6 correspond to $\mu(H_2O)$ in gas and bulk liquid phases, respectively.

On the reconstructed GaP(111) surface, $\theta = 1$ ML coverage and 66% H_2O dissociation is thermodynamically favored across the entire accessible $\mu(H_2O)$ range (Figure 6A). Similar to the GaP(110) surface,[12,13] the dissociated structure is stabilized by a number of favorable interactions, as shown in Figures 6 and S3. H_2O and OH^- molecules bond at Ga sp^2 sites (with Ga−O bond lengths of ∼2.0 Å), H^+'s bond with P lone pairs (with P−H bond lengths of ∼1.4 Å), and dissociated OH^- groups are stabilized by hydrogen bonds with the remaining nondissociated H_2O molecules (all at ∼1.6 Å). The interaction between water and the reconstructed CdTe(111) surface is much weaker, where H_2O adsorption only occurs near the water-rich limit (Figure 6B). Cd is significantly less electronegative than Ga, which leads to a comparatively weaker interaction between the empty p orbital of Cd and the lone pair of adsorbed H_2O or OH^-. Furthermore, water dissociation is unfavorable on the CdTe(111) surface, as dissociation results in significant distortions of the surface structure (Figure S4). Accordingly, the thermodynamically favored structure corresponds to a high coverage at $\theta = 2$ ML with 0% dissociation, where the lattice spacing of CdTe(111) allows nondissociated H_2O molecules to form a stable hexamer (Figure 6D). This structure is less stable on the GaP(111) surface, where the smaller lattice spacing of GaP(111) leads to steric crowding when forming an equivalent hexamer (Figure S3J). The GaP(111) surface at $\theta = 1$ ML with 66% dissociation and the CdTe(111) surface at $\theta = 2$ ML with 0% dissociation are thermodynamically favored under water-rich conditions and therefore are used to determine the CBMs of the solvated electrode surfaces. All water adsorption geometries are provided in Figures S3 and S4 of the Supporting Information.

The adsorption/dissociation geometries shown in Figure 6 are used in conjunction with a previously developed methodology[21,32] to determine CBM positions relative to vacuum. In this methodology, a DFT-PBE calculation using a slab model (i.e., the optimized structure of the solvated GaP(111) or CdTe(111) surface) is used to determine the position of the band gap center (E_{BGC}) relative to vacuum (i.e., the work function determined from the electrostatic potential of the vacuum region). Since DFT-PBE fails to adequately describe the magnitude of the band gap, a non-self-consistent PBE/G_0W_0 calculation using a bulk unit cell model is implemented to accurately determine the intrinsic band gap (E_g) of the semiconductor. The CBM is then determined using the relation: $E_{CBM} = E_{BGC} + 1/2E_g$, which can be related to the SCE electrochemical scale using the absolute potential of the SHE (i.e., $V_{CBM/SCE} = -E_{CBM/Vacuum} - 4.281\text{ V} - 0.244\text{ V}$). The intrinsic band gap of GaP was calculated in our previous work,[21] in which G_0W_0 calculations resulted in a value of E_g = 2.47 eV where the experimentally[54] determined band gap is 2.22 eV. In the present work, G_0W_0 yields a CdTe band gap of E_g = 1.31 eV, consistent with previously reported[55,56] theoretical (PBE/GW_0) and experimental values of 1.44 eV and 1.45 eV, respectively. We obtain a value of E_{BGC} = −4.08 eV relative to the vacuum potential of solvated GaP(111), which results in a CBM at −2.85 eV (Figure S5). Likewise for the CdTe(111) surface, we find that E_{BGC} = −3.86 eV, yielding a CBM at −3.21 eV relative to vacuum. We assign the above CBM positions to pH = 7, which we consider to be the point of zero charge of the surface, as justified previously.[21] To account for band edge shifts induced by changes in the solution pH, we use the well-known Nernst relation:

$$E_{CBM}[pH] = E_{CBM}[pH_{zc}] + 0.059\cdot(pH - pH_{zc}) \quad (6)$$

to adjust the CBM to reflect different pH values. This yields the band edge positions reported in Table 1, where the CBMs of −3.26 eV and −3.62 eV at pH = 0 for GaP(111) and CdTe(111), respectively, are in good agreement with the analogous theoretically predicted values of −3.19 eV and −3.55

Table 1. CBM Positions of the Solvated, Reconstructed GaP(111), and CdTe(111) Surfaces[a]

	GaP(111)	CdTe(111)
pH = 0	−3.26	−3.62
	−1.27	*−0.91*
pH = 5.2	−2.95	−3.31
	−1.58	*−1.22*
pH = 7	−2.85	−3.21
	−1.68	*−1.32*

[a] Regular-font values are reported in eV vs vacuum, and italicized-font values are in V vs SCE.

eV reported by Chen et al.[57] In the following section, we compare these CBM positions to reduction potentials calculated with cluster models of the reconstructed semiconductor surfaces.

3.3. Adsorption Trends and Reduction Potentials Evaluated with Cluster Models. The cluster models employed in the following section were benchmarked against periodic surface models, as discussed in the Supporting Information (Figure S6). Adsorption free energies at 298 K for solvated species on the reconstructed GaP(111) and CdTe(111) surfaces are reported in Figure 7, along with previously reported[21] adsorption energies on the GaP(110) surface. All adsorption geometries are provided in Figures S7 and S8. Under ambient conditions, Py and DHP will spontaneously adsorb on all of the investigated electrode surfaces, with Py adsorption energies of −0.40 eV, −0.31 eV, and −0.04 eV and DHP adsorption energies of −0.35 eV, −0.25 eV, and −0.11 eV on GaP(110), GaP(111), and CdTe(111), respectively. Favorable interactions in this case result from donor−acceptor bonding between the nitrogen lone pair and the empty p orbital located on the sp^2 cation site, with bond lengths of ~2.2 Å and ~2.3 Å for Py and DHP, respectively. The protonated PyH^+ species has no available nitrogen lone pair for donor−acceptor bonding, resulting in positive adsorption energies of 0.24, 0.25, and 0.13 eV on GaP(110), GaP(111), and CdTe(111), respectively. Here, the π-orbitals of the aromatic PyH^+ ring weakly interact with the empty cation p orbitals, leading to a planar adsorption geometry parallel to the surface (Figures S7B and S8B). However, this interaction is not significant enough to overcome strong stabilization of $PyH^+_{(aq)}$ by solvation in the aqueous phase. Attempts to optimize a binding geometry with the protic hydrogen of PyH^+ oriented toward the lone-pair of P or Te failed, resulting in the planar adsorption geometry seen in the figure. CO_2 also does not spontaneously adsorb, where weak dispersive interactions do not alter the linear geometry of the molecule (Figures S7G and S8G). As discussed above, H_2O forms a donor−acceptor bond with the surface, although this binding is weak at low coverages where there is no stabilization from neighboring H_2O molecules (Figures S7H and S8H). H binds at the exposed lone-pair of the sp^3 anion site, where a change in the local geometry of the neighboring cation from planar/sp^2 to pyramidal/sp^3 indicates that the cation is reduced upon H adsorption (Figures S7I and S8I). Localization of charge on the neighboring cation accounts for weaker H adsorption on the CdTe(111) surface, since the less electronegative Cd atom does not readily accept the additional electron.

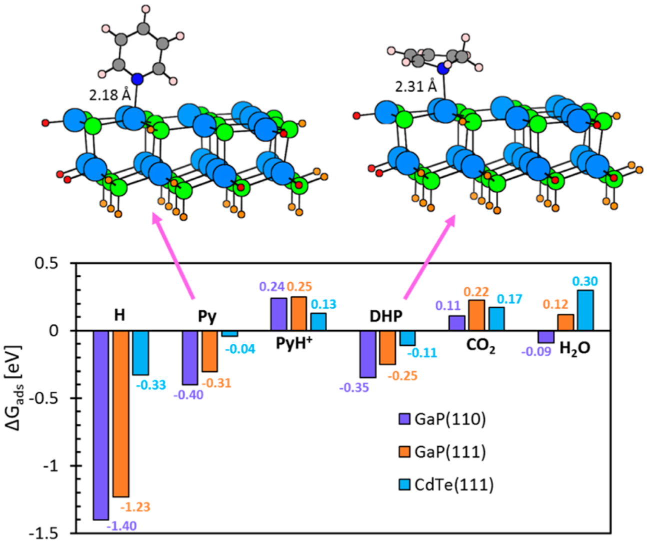

Figure 7. Adsorption free energies on reconstructed GaP(111) and CdTe(111) surfaces compared to previously[21] calculated data on a cluster model of the GaP(110) surface. The insets show the optimized binding geometry of Py and DHP on the GaP(111) cluster model. Further details regarding binding geometries of all species on both GaP(111) and CdTe(111) are provided in the Supporting Information.

These trends offer insight into the observed difference in performance between the varying electrode surfaces. Generally, H- and Py-derived species bind more strongly to GaP(110) compared to GaP(111), indicating that these species will form more readily on the GaP(110) surface. This would account for the increase in current density reported when the GaP electrode is pretreated to expose GaP(110) facets,[23] as more reduction steps involving adsorption from the aqueous phase will occur. Qualitative differences in adsorption trends also have implications when predicting the relative performance of CdTe and GaP. Adsorption, while still exothermic for many Py-derived species, is significantly weaker on CdTe compared to the GaP surfaces, indicating that CdTe may be less active as a heterogonous catalyst. In particular, we do not expect any hydride-like species to exist on the CdTe surface, as H adsorption is ~1 eV less favorable on CdTe(111) compared to the GaP surfaces. Hence, reduction mechanisms involving adsorbed Py and DHP species are expected to play a role on both CdTe and GaP, while mechanisms involving surface hydrides are only expected to play a role on GaP surfaces. The source of surface-bound hydrogen atoms in this system is the reduction of protic species from solution, and therefore reduction potentials, as opposed to adsorption energies calculated relative to a hydrogen atom, are the appropriate measure for whether or not a surface-bound H species can form, as will be discussed further below.

In addition to analyzing adsorption free energy trends, we conducted electron density difference (EDD, calculated as ρ[cluster/radical] − ρ[cluster] − ρ[radical]) and Bader charge analyses to assess the charge transfer between Py-derived radicals and the reconstructed electrode surfaces. These calculations were completed using a (4 × 4) periodic slab model of the reconstructed surfaces, as the periodic slab model approach was previously determined[21] to yield charge distributions that are qualitatively similar to those obtained using cluster models with implicit solvation. As discussed in the introduction, we investigated two radical species, 1-$PyH^\bullet$ and 2-$PyH^\bullet$, that may be involved in the CO_2 reduction mechanism. 1-$PyH^\bullet$ adsorbed on both GaP(111) and CdTe(111) is predicted to form a zwitterion with the electrode surface where there is clear negative charge depletion on the adsorbed radical accompanied by negative charge accumulation on the surface cations (Figure 8). This charge transfer is further demonstrated by the summed Bader charges shown in Table 2, where there are electron transfers of 0.21*e* and 0.14*e* from the radical to GaP(111) and CdTe(111), respectively. Again, this is in agreement with expectations, as the weaker electronegativity of Cd results in less significant electron transfer from the radical to CdTe(111) compared to what is observed on GaP(111).

DOI: 10.1021/acs.chemmater.6b02084
Chem. Mater. 2016, 28, 5799−5810

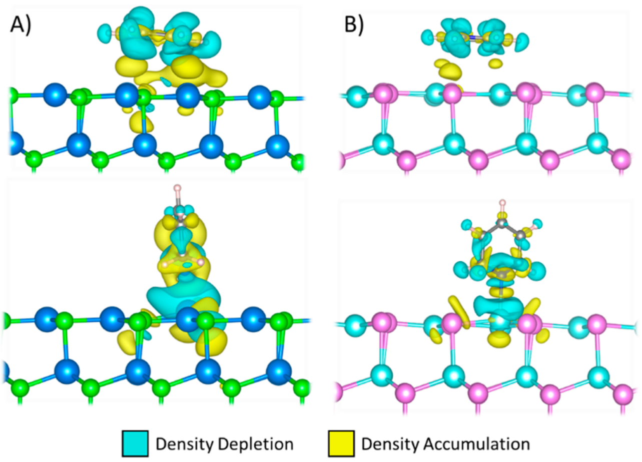

Figure 8. Electron density difference plots of adsorbed 1-PyH$^•$ (top) and 2-PyH$^•$ (bottom) radicals on the (A) GaP(111) and (B) CdTe(111) reconstructed surfaces. Ga atoms are shown in dark blue, P atoms are shown in green, Cd atoms are shown in light blue, and Te atoms are shown in pink. The isosurface level of charge accumulation and depletion is 0.001 e$^-$ bohr^{-3}.

Table 2. Bader Charge Difference of Adsorbed 1-PyH$^•$ and 2-PyH$^•$ Radicals (Units of *e*, Where a Negative (Positive) Value Indicates a Loss (Gain) of Electrons)

	1-PyH$^•$	2-PyH$^•$
GaP(111)	molecule: −0.21	molecule: + 0.05
	surface: + 0.21	surface: −0.05
CdTe(111)	molecule: −0.14	molecule: −0.07
	surface: + 0.14	surface: + 0.07

For the 2-PyH$^•$ radical adsorbed on GaP(111), we obtain a result that is qualitatively different. The Bader charge differences, reported in Table 2, indicate a modest electron transfer of 0.05*e* from the surface to the radical. As seen in Figure 8, there is no clear depletion of charge localized on the adsorbed radical, where there is an apparent accumulation of charge on H atoms at the second position of the Py ring (i.e., indicating that these hydrogens are hydridic in nature). This suggests that it is possible for the 2-PyH$^•$ radical to exist on the GaP(111) surface and that such a species can serve as an active hydride source. On CdTe(111), however, it is less clear that the 2-PyH$^•$ radical will be stable, as the predicted electron transfer from the radical to the surface (0.07*e*) is similar in magnitude to what is predicted for 1-PyH$^•$ (0.14*e*). On the basis of these results, we conclude that the 1-PyH$^•$ radical will not be stable on either electrode, while it may be feasible for the 2-PyH$^•$ radical to exist on the GaP(111) surface. Reduction potentials reported in the following will establish whether or not it is thermodynamically feasible to form the 2-PyH$^•$ radical by transferring a photoexcited electron from the CBM of the solvated electrode surface.

Figure 9 summarizes calculated reduction potentials plotted against the CBMs of the solvated surfaces. The alignment of the CBM determines whether each particular reduction step is thermodynamically feasible given the energy of a photoexcited electron from the semiconductor surface. To elucidate the role of surface adsorption, potentials corresponding to reductions occurring solely in solution are also reported for comparison. We first consider 1e$^-$ reductions of PyH$^+_{(aq)}$, which are thermodynamically equivalent to Py$_{(aq)}$ reductions via proton-coupled-electron-transfer (PCET) when the pH equals the pK_a of PyH$^+_{(aq)}$. The reduction of PyH$^+_{(aq)}$ to 1-PyH$^•_{(aq)}$ in solution occurs at a reduction potential of −1.57 V, which is nearly thermo-neutral with the calculated CBM of solvated GaP(111) at −1.58 V. Although feasible, we contend that this step will be a minor contributor to the overall reduction of PyH$^+_{(aq)}$, as there is little thermodynamic driving force for it to occur. Also, the reverse process, in which the 1-PyH$^{•}$* radical loses an electron back to the electrode surface, can readily occur as demonstrated by the EDD and Bader analyses discussed above. Comparatively, the reduction of PyH$^+_{(aq)}$ to adsorbed 2-PyH$^{•}$* is more favorable, occurring at a potential of −1.46 V, and where EDD and Bader analyses show that the 2-PyH$^{•}$* radical will retain the additional electron. As seen in the figure, 2-PyH$^•$ formation is not feasible in solution (E^0 = −1.78 V), and the adsorbed 2-PyH$^{•}$* species cannot be formed via a PCET from adsorbed Py* (E^0 = −1.76 V). This indicates that an available surface site * must be present to form this species, which could possibly account for the Py poisoning effect noted in experimental studies.[4,6,7] The reduction of PyH$^+_{(aq)}$ to adsorbed Py* + H*, which also requires available surface sites, is significantly more favorable than the formation of either radical species, with a reduction potential of −1.25 V. We thus consider PyH$^+_{(aq)}$ reduction steps resulting in adsorbed species (i.e., either Py* + H* or 2-PyH*) to be favored on the GaP(111) surface over reductions, resulting in the formation of a radical in solution. Also, 2e$^-$ reductions of Py resulting in the formation of DHP* are significantly favored, occurring at potentials ranging from −0.71 V to −0.90 V.

No 1e$^-$ reductions are thermodynamically feasible over the CdTe(111) surface (Figure 9B). This is in part due to a CBM at −1.22 V that lies significantly lower in energy compared to that of GaP(111), which precludes the reduction of PyH$^+_{(aq)}$ either to 1-PyH$^•_{(aq)}$ in solution (E^0 = −1.57 V) or to 2-PyH$^•$ either in solution or adsorbed on the surface (E^0 = −1.78 V and −1.73 V, respectively). The reduction of PyH$^+_{(aq)}$ to adsorbed Py* + H* requires a very negative potential of −2.32 V, which again reflects the highly unfavorable adsorption of H on CdTe(111) attributed to the less electronegative character of Cd. Hence, only 2e$^-$ reductions of Py that result in the formation of DHP via a PCHT are possible provided the energy of photoexcited electrons from the CdTe(111) CBM, which occur over potentials ranging from −0.75 V to −0.80 V.

A number of important conclusions may be drawn from the computed reduction potentials over the reconstructed GaP(111) and CdTe(111) surfaces. Numerous 1e$^-$ reductions of PyH$^+_{(aq)}$ are thermodynamically feasible over the GaP(111) surface. However, there is little thermodynamic driving force to form the 1-PyH$^•_{(aq)}$ radical, which if formed is likely to be a short-lived species because charge is readily transferred back to the electrode leading to the subsequent desorption of PyH$^+_{(aq)}$.[10] Instead, formation of the 2-PyH$^{•}$* radical is thermodynamically preferred, where such a species will not transfer charge back to the electrode. Overall, the most favorable 1e$^-$ reduction corresponds to the formation of adsorbed Py* + H*,[21] which generates the precursors necessary for DHP* formation via HT from the surface and PT from the solution.[14,15] We therefore conclude that reduction events involving surface adsorption are more likely to occur, where differences in adsorption strength explain the facet-dependent behavior in electrode performance observed by Hu and Bocarsly.[23] Unlike the GaP surfaces, no 1e$^-$ reductions are feasible on the CdTe(111) surface. This is a consequence of a

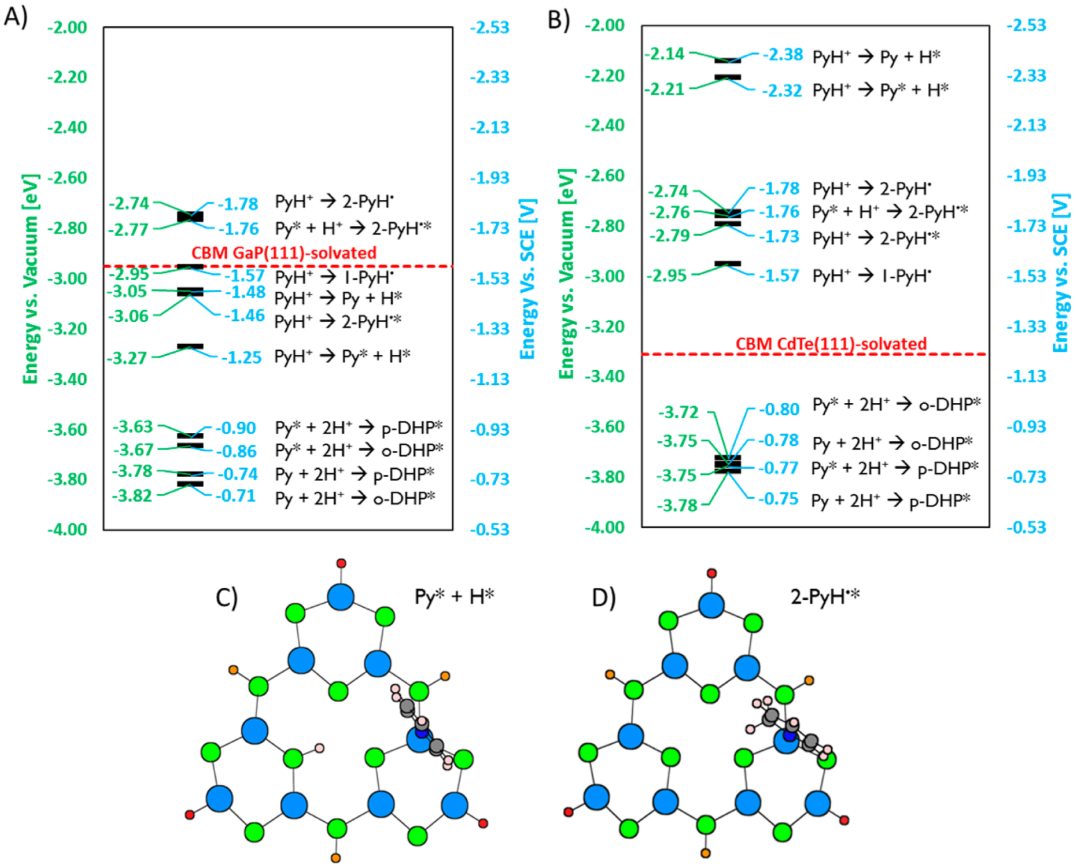

Figure 9. Reduction potentials of possible $PyH^+_{(aq)}$ reduction pathways plotted relative to the CBM of the reconstructed (A) GaP(111) and (B) CdTe(111) surfaces at pH = 5.2. An * indicates that the species is adsorbed on the cluster model, where all other species are in solution. (C,D) Optimized geometry of (C) Py* + H* and (D) 2-PyH$^\bullet$* on GaP(111). o-DHP signifies 1,2-dihydropyridine and p-DHP signifies 1,4-dihydropyridine.

low-lying CBM combined with generally weak adsorption energies. However, Py and DHP adsorption are still favorable on this surface, where DHP* may form in a $2e^-/2H^+$ reduction of Py* via a concerted mechanism where the aqueous solution acts as a H^+ source. Overall, this suggests that CdTe(111) will be a less active electrode material, since this $2e^-$ process would likely have a higher kinetic barrier compared to stepwise $1e^-$ reductions leading to DHP* formation on GaP(111).

4. CONCLUSIONS

In this work, we considered reconstructions of polar GaP(111) and CdTe(111) electrode surfaces affecting Py-catalyzed CO_2 photoreduction. Using *ab initio* thermodynamics to compute the relative free energy of possible surface terminations, we identified stable reconstructions that are likely to occur during catalytic operation. Similar to reconstructions of the GaAs(111) surface,[25] we found that the GaP(111) surface will readily form a (2 × 2) reconstruction with one surface Ga vacancy per unit cell. This reconstruction is closely related to predicted[48] and observed[49] reconstructions of the CdTe(111) surface. Having identified plausible models of the reconstructed electrode surfaces, we then investigated numerous water adsorption and dissociation geometries to identify the most favorable solvent/electrode interfacial structures, allowing us to assess the impact of the solution on the semiconductor band edge alignment. As was observed previously for the GaP(110) surface,[12,13,21] we found that water will readily dissociate on the GaP(111) surface, where dissociated OH^- and H^+ groups are stabilized by donor−acceptor bonds formed at sp^2 Ga and sp^3 P sites, respectively, created by the surface reconstruction. Water does not dissociate on the CdTe(111) surface but rather forms a stable hexamer structure. Using periodic slab models of the explicitly solvated surface to compute work functions from DFT and bulk crystal G_0W_0 calculations to determine accurate band gaps, we derived accurate band edge positions of the solvated electrode under working conditions. These were then compared to $PyH^+_{(aq)}$ reduction potentials calculated with implicitly solvated cluster models of the reconstructed surfaces to determine which reduction steps can occur through the transfer of photoexcited electrons from the CBM of the solvated electrode, lending insight into likely steps of Py-enhanced reduction pathways occurring at the electrode surface.

On the basis of the band edge alignment of the solvated GaP(111) surface, we determined that the $1e^-$ reduction of $PyH^+_{(aq)}$ resulting in the formation of adsorbed Py* + H*, as well as reduction to the newly proposed 2-PyH$^\bullet$* intermediate, is thermodynamically favored over the formation of a 1-$PyH^\bullet_{(aq)}$ radical in solution. Furthermore, differences in calculated adsorbate binding energies between GaP(110) and GaP(111) surfaces likely account for experimentally observed facet-dependent current densities.[23] On the CdTe(111) surface, we found that no $1e^-$ reductions were thermodynamically feasible, leaving only $2e^-$ reductions leading to the formation of DHP as plausible reduction steps. This suggests that there should be an observable difference in electrode performance between GaP and CdTe, where GaP is expected to yield higher current densities since more reduction steps are feasible. At the same time, GaP may exhibit lower Faradaic efficiencies compared to CdTe since more side reactions are feasible.

■ ASSOCIATED CONTENT

Supporting Information

The Supporting Information is available free of charge on the ACS Publications website at DOI: 10.1021/acs.chemmater.6b02084.

> Additional calculation details, benchmark data for cluster models, structural figures, and Cartesian coordinates and total DFT energies of geometries discussed in the text (PDF)

■ AUTHOR INFORMATION

Corresponding Author

*E-mail: eac@princeton.edu.

Notes

The authors declare no competing financial interest.

■ ACKNOWLEDGMENTS

The authors acknowledge financial support from the Air Force Office of Scientific Research under AFOSR Award No. FA9550-10-1-0572 and are grateful to Dr. Johannes Dieterich and Ms. Nari Baughman for helping to revise the manuscript.

■ REFERENCES

(1) White, J. L.; Baruch, M. F.; Pander, J. E., III; Hu, Y.; Fortmeyer, I. C.; Park, J. E.; Zhang, T.; Liao, K.; Gu, J.; Yan, Y.; Shaw, T. W.; Abelev, E.; Bocarsly, A. B. Light-Driven Heterogeneous Reduction of Carbon Dioxide: Photocatalysts and Photoelectrodes. *Chem. Rev.* **2015**, *115*, 12888−12935.

(2) Barton, E. E.; Rampulla, D. M.; Bocarsly, A. B. Selective Solar-Driven Reduction of CO2 to Methanol Using a Catalyzed p-GaP Based Photoelectrochemical Cell. *J. Am. Chem. Soc.* **2008**, *130*, 6342−6344.

(3) Barton Cole, E.; Lakkaraju, P. S.; Rampulla, D. M.; Morris, A. J.; Abelev, E.; Bocarsly, A. B. Using a One-Electron Shuttle for the Multielectron Reduction of CO2 to Methanol: Kinetic, Mechanistic, and Structural Insights. *J. Am. Chem. Soc.* **2010**, *132*, 11539−11551.

(4) Jeon, J. H.; Mareeswaran, P. M.; Choi, C. H.; Woo, S. I. Synergism between CdTe semiconductor and pyridine - photoenhanced electrocatalysis for CO2 reduction to formic acid. *RSC Adv.* **2014**, *4*, 3016−3019.

(5) Yuan, J.; Hao, C. Solar-driven photoelectrochemical reduction of carbon dioxide to methanol at CuInS2 thin film photocathode. *Sol. Energy Mater. Sol. Cells* **2013**, *108*, 170−174.

(6) Yuan, J.; Zheng, L.; Hao, C. Role of pyridine in photoelectrochemical reduction of CO2 to methanol at a CuInS2 thin film electrode. *RSC Adv.* **2014**, *4*, 39435−39438.

(7) Yuan, J.; Wang, P.; Hao, C.; Yu, G. Photoelectrochemical reduction of carbon dioxide at CuInS2/graphene hybrid thin film electrode. *Electrochim. Acta* **2016**, *193*, 1−6.

(8) Tossell, J. A. Calculation of the properties of molecules in the pyridine catalyst system for the photochemical conversion of CO2 to methanol. *Comput. Theor. Chem.* **2011**, *977*, 123−127.

(9) Keith, J. A.; Carter, E. A. Theoretical Insights into Pyridinium-Based Photoelectrocatalytic Reduction of CO2. *J. Am. Chem. Soc.* **2012**, *134*, 7580−7583.

(10) Keith, J.; Muñoz-García, A.; Lessio, M.; Carter, E. Cluster Models for Studying CO2 Reduction on Semiconductor Photoelectrodes. *Top. Catal.* **2015**, *58*, 46−56.

(11) Keith, J. A.; Carter, E. A. Electrochemical reactivities of pyridinium in solution: consequences for CO2 reduction mechanisms. *Chem. Sci.* **2013**, *4*, 1490−1496.

(12) Muñoz-García, A. B.; Carter, E. A. Non-innocent Dissociation of H2O on GaP(110): Implications for Electrochemical Reduction of CO2. *J. Am. Chem. Soc.* **2012**, *134*, 13600−13603.

(13) Kronawitter, C. X.; Lessio, M.; Zhao, P.; Riplinger, C.; Boscoboinik, A.; Starr, D. E.; Sutter, P.; Carter, E. A.; Koel, B. E. Observation of Surface-Bound Negatively Charged Hydride and Hydroxide on GaP(110) in H2O Environments. *J. Phys. Chem. C* **2015**, *119*, 17762−17772.

(14) Keith, J. A.; Carter, E. A. Theoretical Insights into Electrochemical CO2 Reduction Mechanisms Catalyzed by Surface-Bound Nitrogen Heterocycles. *J. Phys. Chem. Lett.* **2013**, *4*, 4058−4063.

(15) Keith, J. A.; Carter, E. A. Correction to "Theoretical Insights into Electrochemical CO2 Reduction Mechanisms Catalyzed by Surface-Bound Nitrogen Heterocycles. *J. Phys. Chem. Lett.* **2015**, *6*, 568−568.

(16) Lim, C.-H.; Holder, A. M.; Hynes, J. T.; Musgrave, C. B. Reduction of CO2 to Methanol Catalyzed by a Biomimetic Organo-Hydride Produced from Pyridine. *J. Am. Chem. Soc.* **2014**, *136*, 16081−16095.

(17) Lim, C.-H.; Holder, A. M.; Hynes, J. T.; Musgrave, C. B. Catalytic Reduction of CO2 by Renewable Organohydrides. *J. Phys. Chem. Lett.* **2015**, *6*, 5078−5092.

(18) Ertem, M. Z.; Konezny, S. J.; Araujo, C. M.; Batista, V. S. Functional Role of Pyridinium during Aqueous Electrochemical Reduction of CO2 on Pt(111). *J. Phys. Chem. Lett.* **2013**, *4*, 745−748.

(19) Zeitler, E. L.; Ertem, M. Z.; Pander, J. E.; Yan, Y.; Batista, V. S.; Bocarsly, A. B. Isotopic Probe Illuminates the Role of the Electrode Surface in Proton Coupled Hydride Transfer Electrochemical Reduction of Pyridinium on Pt(111). *J. Electrochem. Soc.* **2015**, *162*, H938−H944.

(20) Yan, Y.; Zeitler, E. L.; Gu, J.; Hu, Y.; Bocarsly, A. B. Electrochemistry of Aqueous Pyridinium: Exploration of a Key Aspect of Electrocatalytic Reduction of CO2 to Methanol. *J. Am. Chem. Soc.* **2013**, *135*, 14020−14023.

(21) Lessio, M.; Carter, E. A. What Is the Role of Pyridinium in Pyridine-Catalyzed CO2 Reduction on p-GaP Photocathodes? *J. Am. Chem. Soc.* **2015**, *137*, 13248−13251.

(22) Landis, C. Private Communication, 2016.

(23) Hu, Y.; Bocarsly, A. B. Doctoral Thesis, Princeton University, 2015.

(24) Lide, D. R. *Handbook of Chemistry and Physics: A Ready Reference Book of Chemical and Physical Data*, 84 ed.; CRC Press: New York, 2004.

(25) Moll, N.; Kley, A.; Pehlke, E.; Scheffler, M. GaAs equilibrium crystal shape from first principles. *Phys. Rev. B: Condens. Matter Mater. Phys.* **1996**, *54*, 8844−8855.

(26) Kresse, G.; Furthmuller, J. Efficiency of ab-initio total energy calculations for metals and semiconductors using a plane-wave basis set. *Comput. Mater. Sci.* **1996**, *6*, 15−50.

(27) Perdew, J. P.; Burke, K.; Ernzerhof, M. Generalized Gradient Approximation Made Simple. *Phys. Rev. Lett.* **1996**, *77*, 3865−3868.

(28) Grimme, S. Semiempirical GGA-type density functional constructed with a long-range dispersion correction. *J. Comput. Chem.* **2006**, *27*, 1787−1799.

(29) Blöchl, P. E. Projector augmented-wave method. *Phys. Rev. B: Condens. Matter Mater. Phys.* **1994**, *50*, 17953−17979.

(30) Monkhorst, H. J.; Pack, J. D. Special points for Brillouin-zone integrations. *Phys. Rev. B* **1976**, *13*, 5188−5192.

(31) Onida, G.; Reining, L.; Rubio, A. Electronic excitations: density-functional versus many-body Green's-function approaches. *Rev. Mod. Phys.* **2002**, *74*, 601−659.

(32) Toroker, M. C.; Kanan, D. K.; Alidoust, N.; Isseroff, L. Y.; Liao, P.; Carter, E. A. First principles scheme to evaluate band edge positions in potential transition metal oxide photocatalysts and photoelectrodes. *Phys. Chem. Chem. Phys.* **2011**, *13*, 16644−16654.

(33) Valiev, M.; Bylaska, E. J.; Govind, N.; Kowalski, K.; Straatsma, T. P.; Van Dam, H. J. J.; Wang, D.; Nieplocha, J.; Apra, E.; Windus, T. L.; de Jong, W. A. NWChem: A comprehensive and scalable open-source solution for large scale molecular simulations. *Comput. Phys. Commun.* **2010**, *181*, 1477−1489.

(34) Lee, C.; Yang, W.; Parr, R. G. Development of the Colle-Salvetti correlation-energy formula into a functional of the electron density. *Phys. Rev. B: Condens. Matter Mater. Phys.* **1988**, *37*, 785−789.

(35) Becke, A. D. Density-functional exchange-energy approximation with correct asymptotic behavior. *Phys. Rev. A: At., Mol., Opt. Phys.* **1988**, *38*, 3098−3100.

(36) Marenich, A. V.; Cramer, C. J.; Truhlar, D. G. Universal Solvation Model Based on Solute Electron Density and on a Continuum Model of the Solvent Defined by the Bulk Dielectric Constant and Atomic Surface Tensions. *J. Phys. Chem. B* **2009**, *113*, 6378−6396.

(37) Bergner, A.; Dolg, M.; Küchle, W.; Stoll, H.; Preuß, H. Ab initio energy-adjusted pseudopotentials for elements of groups 13−17. *Mol. Phys.* **1993**, *80*, 1431−1441.

(38) Leininger, T.; Berning, A.; Nicklass, A.; Stoll, H.; Werner, H.-J.; Flad, H.-J. Spin-orbit interaction in heavy group 13 atoms and TlAr. *Chem. Phys.* **1997**, *217*, 19−27.

(39) Francl, M. M.; Pietro, W. J.; Hehre, W. J.; Binkley, J. S.; Gordon, M. S.; DeFrees, D. J.; Pople, J. A. Self-consistent molecular orbital methods. XXIII. A polarization-type basis set for second-row elements. *J. Chem. Phys.* **1982**, *77*, 3654−3665.

(40) Dunning, T. H. Gaussian basis sets for use in correlated molecular calculations. I. The atoms boron through neon and hydrogen. *J. Chem. Phys.* **1989**, *90*, 1007−1023.

(41) Isse, A. A.; Gennaro, A. Absolute Potential of the Standard Hydrogen Electrode and the Problem of Interconversion of Potentials in Different Solvents. *J. Phys. Chem. B* **2010**, *114*, 7894−7899.

(42) Tissandier, M. D.; Cowen, K. A.; Feng, W. Y.; Gundlach, E.; Cohen, M. H.; Earhart, A. D.; Coe, J. V.; Tuttle, T. R. The Proton's Absolute Aqueous Enthalpy and Gibbs Free Energy of Solvation from Cluster-Ion Solvation Data. *J. Phys. Chem. A* **1998**, *102*, 7787−7794.

(43) Tasker, P. W. The stability of ionic crystal surfaces. *J. Phys. C: Solid State Phys.* **1979**, *12*, 4977−4984.

(44) Pashley, M. D. Electron counting model and its application to island structures on molecular-beam epitaxy grown GaAs(001) and ZnSe(001). *Phys. Rev. B: Condens. Matter Mater. Phys.* **1989**, *40*, 10481−10487.

(45) Chetty, N.; Martin, R. M. Determination of integrals at surfaces using the bulk crystal symmetry. *Phys. Rev. B: Condens. Matter Mater. Phys.* **1991**, *44*, 5568−5571.

(46) Kaxiras, E.; Pandey, K. C.; Bar-Yam, Y.; Joannopoulos, J. D. Role of chemical potentials in surface reconstruction: A new model and phase transition of GaAs(111)2 × 2. *Phys. Rev. Lett.* **1986**, *56*, 2819−2822.

(47) Tong, S. Y.; Xu, G.; Mei, W. N. Vacancy-Buckling Model for the GaAs(111) Surface. *Phys. Rev. Lett.* **1984**, *52*, 1693−1696.

(48) Li, J.; Kioussis, N.; Aqariden, F.; Grein, C. Thermodynamic and stoichiometric stability of the Cd-terminated CdTe (111) surface. *Phys. Rev. B: Condens. Matter Mater. Phys.* **2012**, *85*, 235306.

(49) Egan, C. K.; Jiang, Q. Z.; Brinkman, A. W. Morphology and reconstructions of polar CdTe(111)A,B surfaces by scanning tunneling microscopy. *J. Vac. Sci. Technol., A* **2011**, *29*, 011021.

(50) Evans, H. Crystal Structure of Low Chalcocite. *Nature, Phys. Sci.* **1971**, *232*, 69−70.

(51) Bosio, L.; Defrain, A.; Curien, H.; Rimsky, A. Crystal Structure of Gallium-beta. *Acta Crystallogr., Sect. B: Struct. Crystallogr. Cryst. Chem.* **1969**, *25*, 995.

(52) Kharche, N.; Muckerman, J. T.; Hybertsen, M. S. First-Principles Approach to Calculating Energy Level Alignment at Aqueous Semiconductor Interfaces. *Phys. Rev. Lett.* **2014**, *113*, 176802.

(53) Kharche, N.; Hybertsen, M. S.; Muckerman, J. T. Computational investigation of structural and electronic properties of aqueous interfaces of GaN, ZnO, and a GaN/ZnO alloy. *Phys. Chem. Chem. Phys.* **2014**, *16*, 12057−12066.

(54) Zallen, R.; Paul, W. Band Structure of Gallium Phosphide from Optical Experiments at High Pressure. *Phys. Rev.* **1964**, *134*, A1628−A1641.

(55) Hinuma, Y.; Grüneis, A.; Kresse, G.; Oba, F. Band alignment of semiconductors from density-functional theory and many-body perturbation theory. *Phys. Rev. B: Condens. Matter Mater. Phys.* **2014**, *90*, 155405.

(56) Grüneis, A.; Kresse, G.; Hinuma, Y.; Oba, F. Ionization Potentials of Solids: The Importance of Vertex Corrections. *Phys. Rev. Lett.* **2014**, *112*, 096401.

(57) Chen, S.; Wang, L.-W. Thermodynamic Oxidation and Reduction Potentials of Photocatalytic Semiconductors in Aqueous Solution. *Chem. Mater.* **2012**, *24*, 3659−3666.